

Article

# Fixed Frequency Sliding Mode Control of Power Converters for Improved Dynamic Response in DC Micro-Grids

Abdul Rehman Yasin <sup>\*</sup>, Muhammad Ashraf  and Aamer Iqbal Bhatti

Department of Electrical Engineering, Capital University of Science and Technology (CUST), Islamabad Expressway, Kahuta Road, Zone-V Islamabad 44000, Pakistan; ashraf@cust.edu.pk (M.A.); aamer987@gmail.com (A.I.B.)

\* Correspondence: metary@gmail.com; Tel.: +92-321-4511396

Received: 30 August 2018; Accepted: 14 October 2018; Published: 17 October 2018



**Abstract:** The rapid decrease in conventional energy resources and their harmful impact on the environment has brought the attention of the researchers towards the use of renewable energy technologies. The renewable energy systems are connected to Direct Current (DC) micro-grids via power electronic converters where the load conditions are unknown and network parameters are uncertain. These conditions call for the use of robust control techniques such as Sliding Mode Control (SMC) in order to regulate the grid voltage. However, SMC has a drawback of operating the power converter at variable switching frequency which results in degrading the power quality. This paper introduces a fixed frequency sliding mode controller that does not suffer from this predicament. A novel double integral type switching manifold is proposed to achieve voltage regulation of a DC micro-grid, in the presence of unknown load demands and un-modeled dynamics of the network. Rigorous mathematical analysis is carried out for the stability of the closed loop system and the technique is experimentally validated on position of a DC micro-grid using a specially designed test rig. For benchmarking purposes, a conventional Proportional Integral (PI) controller is also implemented. An improvement of 2.5% in rise time, 6.7% in settling time and reduction of voltage dip by 31.7% during load transaction is achieved as compared to the PI controller. The experiment confirms the hypothesis that fixed frequency SMC shows better performance than its counterpart in the phase of introduced disturbances.

**Keywords:** DC micro-grids; DC–DC converters; power engineering and energy; sliding mode control

## 1. Introduction

Exponential increase in the energy demand due to massive industrial growth and urbanization has called for the installation of new generation units. To increase the reliability of the system and reduce the probability of complete black out, the researchers are focusing on the development and integration of Distributed power Generation Units (DGU) [1–4]. Moreover, the alarming momentum at which the conventional energy resources are being depleted to meet the power demand motivated the use of Renewable Energy Resources (RER). However, as several DGUs are connected together, issues like voltage regulation and current sharing arise along with protection problems. To address these issues for the large scale integration of RERs, the so-called concept of micro-grids has emerged in the field of power systems. The micro-grid is a power distribution network that consists of DGU clusters, different types of loads, energy storage units and energy conversion devices interconnected via power distribution lines.

Among different types of RERs, solar energy is the most abundant source and researchers are focusing on developing more efficient photo-voltaic cells to achieve the concept of green energy [5,6].

Most of the renewable energy resources, like fuel cells and Photo-Voltaic (PV) cells, are Direct Current (DC) in nature. The energy storage banks use super capacitors, Li-ion, lead-acid and Ni-Cd batteries, which can store energy only in DC form. Other renewable resources like wind mills and bio-gas installations are also DC friendly. On the consumer side, the variable speed drives of induction motors, LEDs and electronic circuitry operate at DC voltages.

Connecting RERs and energy storage banks to Alternating Current (AC) micro-grids requires multiple conversions (DC–AC and AC–DC) that result in unwanted power loss and reduced efficiency [7,8]. To resolve this issue, DC micro-grids have attracted the attention of the researchers [9–13]. Furthermore, skin effect losses are not present in DC micro-grids and the control of DC micro-grids is less complex as compared to AC micro-grids, where issues of frequency regulation and synchronization, flow of reactive power, unwanted harmonics and unbalanced load are the key issues [14–18].

Different energy generation units located at distributed locations are connected to DC micro-grid using DC–DC power electronic converters as shown in Figure 1. The major control problems in this scenario are the voltage regulation and the current sharing among different power sources. Voltage regulation is required for the proper functioning of the load devices, while current sharing is required to ensure that no source is overstressed. These objectives are achieved simultaneously by using a hierarchical control [19–21]. Conventionally Proportional Integral Derivative (PID) controllers are used in the voltage and current control loops of these power electronic converters [22]. However, under uncertain load conditions, the gains of the PID controllers require periodic tuning to give the desired performance [23]. The researchers have proposed auto-tuning methods [24] and Fuzzy controllers [25,26] to achieve better results. However, these methods are system dependent and add complexity to the design.

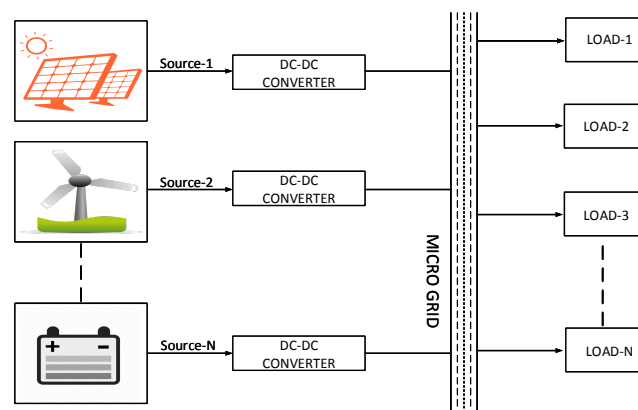


**Figure 1.** Connection of distributed energy resources to a Direct Current (DC) micro-grid.

It is reported that the performance improvement is achieved by using boundary layer control [27–29], adaptive nonlinear control [30], model predictive control [31–33], and a time delayed based robust controller [34]. However, these techniques are not completely parameter independent and require some knowledge of the system specifications like inductance of the coil and capacitance of the filter stage. This calls for the need of a robust controller that can control the nonlinear dynamics of the power converter in order to tightly regulate the voltage in the presence of unknown load demands and uncertain grid parameters.

Indeed, the robustness and parameter invariance [35,36] of Sliding Mode Control (SMC) is well known and makes it an attractive choice for voltage and current control in micro-grids, where load conditions are unknown and network parameters are subject to variations [37–43]. SMC based techniques result in better voltage regulation in the presence of parametric variations, modeling uncertainties and external disturbances [44–46]. However, the major drawback of SMC is its variable switching frequency. Power electronic converters require to operate at fixed switching frequency in

order to minimize switching losses [47] and to suppress Electro-Magnetic Interference (EMI) [48]. Hence, the researchers are motivated to combine the advantages of fixed frequency with the robust nature of SMC [49–54], thereby reducing EMI emissions and switching losses simultaneously.

However, these techniques are implemented on a single DC–DC converter. To the best of the authors' knowledge, the behavior of fixed frequency SMC has not been observed yet on the position of a micro-grid.

To fill the above-mentioned research gap, this paper presents a fixed frequency SMC based approach to track the reference voltage of each source connected to the micro-grid. The proposed technique achieves the desired performance by controlling a boost converter that regulates the grid voltage and ensures proper current sharing in the presence of un-modeled dynamics caused by uncertain load and line variations without using observers, which add cost and complexity to the design. The paper contributes in the following three dimensions:

1. Improving the dynamic response of the closed loop system and increasing the robustness against unknown load demands in a DC micro-grid, using fixed frequency SMC.
2. Designing a novel sliding manifold that results in stable operation of boost converter for wide range of gains, followed by a rigorous mathematical analysis for the stability condition.
3. Designing a special test rig with three sources, in order to validate the results in comparison with conventional PI controllers. Moreover, the technique is also tested for fault condition at one of the sources connected to the micro-grid.

It is important to mention that, in case of micro-grids, the electromagnetic interference (EMI) caused by the power lines and switching of the large inductor current, makes the environment less feasible for the use of Digital Signal Processors (DSP) and Field-Programmable Gate Array (FPGA) boards. Therefore, these boards are used in such applications along with specially designed electromagnetic shielding mechanisms to avoid interference from high frequency switching currents. Moreover, they need additional line filters to permit their interaction with the power lines. Due to these reasons, the proposed technique is demonstrated using low cost commercially available analogue Integrated Circuits (ICs), which present a workable industrial solution without involving A/D converters and DSP/FPGA boards which are less immune to EMI and also add additional cost to the design. Moreover, the analogue implementation gives a better picture of the controller design and its implementation procedure.

The article is arranged as follows: mathematical model of the system and controller design are presented in Sections 2 and 3, respectively. The condition for the existence of sliding mode is described in Section 4. The design of sliding surface and parameterization of the controller is presented in Section 5. The experimental results and discussions are presented in Section 6 while the article is concluded in Section 7.

## 2. Mathematical Model of the System

Each source in the DC micro grid comprises of a DC–DC converter as shown in Figure 2, where input voltage from the renewable energy source is denoted by  $V_{in}$ ,  $I_L$  is the instantaneous inductor current,  $V_{out}$  is the output voltage of the converter,  $R_{load}$  is the load resistance,  $C$  is the capacitance of the output filter capacitor while  $L$  is the inductance of the coil. By using circuit analysis techniques, the nonlinear dynamic model of the system is written as:

$$\begin{aligned} \dot{I}_L &= -(1-u)\frac{1}{L}V_{out} + \frac{(V_{in+\delta n})}{L}, \\ \dot{V}_{out} &= (1-u)\frac{1}{C}I_L - \frac{1}{(R_{load} + \Delta R_{esr})C}V_{out}, \end{aligned} \quad (1)$$

where  $\delta n$  is an unknown but bounded time varying disturbance, which satisfies the condition  $|\delta n| < V_{in}$ ;  $\Delta R_{esr}$  represents the parameter uncertainty caused by Equivalent Series Resistance (ESR)

of the capacitor. Since the power electronic switch can be either On or Off, thus mathematically the control signal  $u$  belongs to a discrete set:  $u \in \{1, 0\}$ . We define  $\tilde{u} = (1 - u)$ , where the control input  $u$  is defined with respect to the power electronic switch as:

$$u(t) = \begin{cases} 1, & \text{Switch is conducting,} \\ 0, & \text{Switch is open circuit.} \end{cases} \quad (2)$$

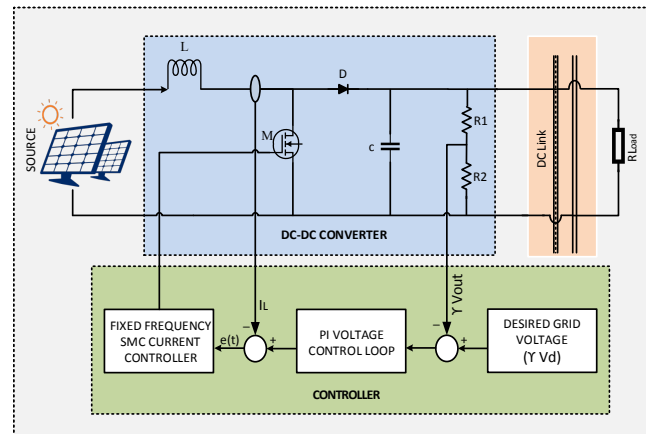


**Figure 2.** Simplified scheme for the voltage and current control using DC–DC boost converter.

The boost converters are nonlinear and non-minimum in-phase with respect to output voltage [55,56] and the dynamics of the inductor current are unstable if the output voltage is considered to be the only variable to be controlled [57]. However, the boost converter satisfies the motion separation principle derived from singular Perturbation Theory [58,59]. It means that the dynamics of  $I_L$  are much faster as compared to the dynamics of  $V_{out}$  and the problem can be solved by designing a cascaded control structure with two control loops. The inner loop controls the inductor current while the outer loop controls the load voltage. The inner control loop is designed using fixed frequency SMC while the outer control loop having slower dynamics is designed using PI controller.

Since the controller is robust; therefore, throughout the article, we consider the simplified model with  $\delta n = 0$  and  $\Delta R_{esr} = 0$ . The section on experimental results and discussion where the input voltage is varied and sudden changes in load are deliberately applied is an exception in order to evaluate the performance of the controller and verify its robustness. The steady state dynamics of the system are found by setting the time derivatives of system states to zero. Thus, as  $t \rightarrow \infty$ ,  $\dot{I}_L = \dot{V}_{out} = 0$  and  $V_{out} = V_d$ . Setting these values in Equation (1), the reference current in the inner loop is derived as:

$$I_{ref}^* = \frac{V_d^2}{R_{load} V_{in}}, \quad (3)$$

where  $I_{ref}^*$  is the reference current for the inner control loop at equilibrium and  $V_d$  is the desired output voltage of the converter.

### 3. Controller Design

The SMC design concept is based upon a discontinuous control law, which directs the system states towards a sliding manifold in the state space. Sliding manifold is designed to insure the finite time convergence of the state trajectories at the origin. The control process of SMC can be segregated into two phases, namely the reaching phase and the sliding phase. During the reaching phase, the controller generates a series of switching commands such that the state trajectories hit the sliding manifold irrespective to their initial conditions as shown in Figure 3a. In the second phase, the controller executes its operation via switching commands, ensuring the trajectory to be in a small

vicinity of the sliding manifold  $\sigma = 0$ , which in turn gets directed concurrently towards the desired reference at the origin 'O' as shown in Figure 3b. In short, the sliding mode operation can be explained such that the controller utilizes the sliding plane as a reference to perform its decisions in order to ensure the convergence of the state trajectories to the origin, where steady state operation is achieved. We select the control law based on the hitting condition [60] as:

$$u = \frac{1}{2}(1 + \text{sign}(\sigma)). \tag{4}$$

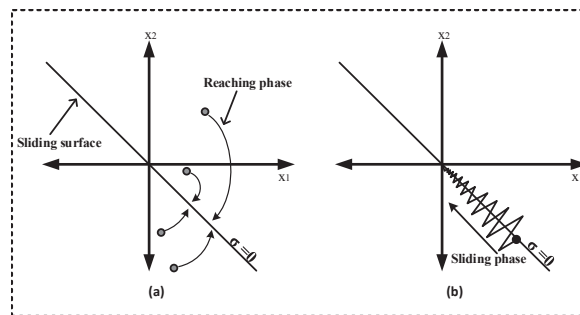


**Figure 3.** State space trajectories under Sliding Mode Control (SMC). (a) reaching phase; (b) sliding phase.

The hitting condition ensures that the state trajectories are always directed towards the sliding manifold  $\sigma = 0$ , regardless of their initial conditions. In order to ensure zero steady state error [61], this paper proposes a double integral type sliding surface given as:

$$\sigma = \lambda_1 \iint e(t)dt dt + \lambda_2 \int e(t)dt + \lambda_3 e(t), \tag{5}$$

where

$$e(t) = I_{ref} - I_L \tag{6}$$

and  $\lambda_1, \lambda_2$  and  $\lambda_3$  are positive design constants. When the state trajectories reach the manifold  $\sigma = 0$ , sliding mode is said to be established. Now onwards, the system becomes parameter invariant [60] and its behavior is described as:

$$\sigma = \lambda_1 \iint e(t)dt dt + \lambda_2 \int e(t)dt + \lambda_3 e(t) = 0, \tag{7}$$

we differentiate Equation (7) w.r.t time and get:

$$\lambda_3 \ddot{e}(t) + \lambda_2 \dot{e}(t) + \lambda_1 e(t) = 0. \tag{8}$$

The Laplace transform of Equation (8) is:

$$s^2 E(s) + s \frac{\lambda_2}{\lambda_3} E(s) + \frac{\lambda_1}{\lambda_3} E(s) = 0. \tag{9}$$

Since  $\lambda_1, \lambda_2$  and  $\lambda_3$  are positive design constants, hence the Laplace transform in Equation (9) is a Hurwitz polynomial and both of the roots lie on the left side of the S-plane. Hence, as  $t \rightarrow \infty$ ,  $e(t) \rightarrow 0$  and  $V_{out} \rightarrow V_d$ .

Implementation of SMC using Pulse Width Modulation (PWM) is based upon two well known theorems. The first theorem [60] states that the discontinuous control  $u$  in SMC can be replaced theoretically with a smooth and continuous time function called equivalent control signal, such that  $0 < u_{eq} < 1$ . The second theorem states that, at sufficiently high frequency, the equivalent control coincides with the duty ratio of the PWM control [62].

The equivalent control  $u_{eq}$  of the system under sliding mode is derived by substituting the time derivative of the sliding surface equal to zero. Thus, setting  $\dot{\sigma} = 0$ , we get:

$$\dot{\sigma} = \lambda_1 \int e(t) dt + \lambda_2 e(t) + \lambda_3 \dot{e}(t) = 0. \quad (10)$$

Involving the dynamics of the system from Equation (1) and rearranging the terms, we get:

$$\tilde{u}_{eq} = \frac{V_{in}}{V_{out}} - L \frac{\lambda_2}{\lambda_3} \frac{e(t)}{V_{out}} - L \frac{\lambda_1}{\lambda_3} \frac{\int e(t) dt}{V_{out}}. \quad (11)$$

Substituting  $\tilde{u} = (1 - u)$ , the expression of  $u_{eq}$  is derived from Equations (6) and (11) as:

$$u_{eq} = \left(1 - \frac{V_{in}}{V_{out}}\right) + L \frac{\lambda_2}{\lambda_3} \frac{(I_{ref} - I_L)}{V_{out}} + \frac{\lambda_1}{\lambda_3} \frac{\int (I_{ref} - I_L) dt}{V_{out}}. \quad (12)$$

Since the equivalent control signal  $u_{eq}$  coincides with the duty ratio  $d$  of PWM converter, we can write:

$$\begin{aligned} u_{eq} &= d = \frac{V_{con}}{V_{Pramp}} \\ \implies V_{con} &= u_{eq} \times V_{Pramp}, \end{aligned} \quad (13)$$

where  $V_{con}$  is the control signal to the PWM modulator and  $V_{Pramp}$  is the peak voltage of ramp signal, respectively. By choosing  $V_{Pramp} = V_{out}$  and using Equation (13), we get:

$$V_{con} = (V_{out} - V_{in}) + L \frac{\lambda_2}{\lambda_3} (I_{ref} - I_L) + L \frac{\lambda_1}{\lambda_3} \int (I_{ref} - I_L) dt, \quad (14)$$

$$V_{Pramp} = V_{out}. \quad (15)$$

It is worth mentioning that the proposed structure in Equation (14) differs from the PI controllers because of the term  $(V_{out} - V_{in})$ . It acts as an adaptive feedforward gain which automatically changes, in an effort to nullify the disturbances in  $V_{in}$ . This adaptation is also reflected in Equation (15) which means that the peak amplitude of the ramp signal is modified in relation with  $V_{out}$ . It acts as an agent to change the modulation index in order to achieve faster dynamic response. Conditions to guarantee stability and avoid over modulation are discussed in Section 4. Another important difference between the two controllers is the way they are designed. The PI controllers are designed on the concept of small signal analysis which makes the response of the system specific to an operating point while sliding mode controllers are large signal systems, where the design is independent from the operating point.

#### 4. Existence of Sliding Mode Control

The existence and stability of SMC is ensured if the control law enforces the state trajectories towards the sliding manifold  $\sigma = 0$ . Mathematically, the following two constraints shall be satisfied in the neighborhood of the manifold:

$$\lim_{\sigma \rightarrow 0^+} \dot{\sigma} < 0, \quad (16)$$

$$\lim_{\sigma \rightarrow 0^-} \dot{\sigma} > 0. \quad (17)$$

For the proposed controller, we obtain the equation for  $\dot{\sigma}$  by using Equations (1) and (5) as:

$$\dot{\sigma} = \lambda_1 x_1(t) + \lambda_2 x_2(t) + \lambda_3 \left( \frac{V_{out}}{L} \tilde{u} - \frac{V_{in}}{L} \right), \quad (18)$$

where  $x_1(t) = \int e(t)dt$  and  $x_2(t) = e(t)$ . The specific conditions for the stable operation of the system are as follows:

Case 1:

When  $\sigma \rightarrow 0^+$ , then Constrain (16) states that  $\dot{\sigma} < 0$ . This turns Equation (18) into an inequality as:

$$\dot{\sigma} = \lambda_1 x_1(t) + \lambda_2 x_2(t) + \lambda_3 \left( \frac{V_{out}}{L} \tilde{u} - \frac{V_{in}}{L} \right) < 0. \quad (19)$$

The control law (4), in Case 1, takes the value  $u = 1$  ( $\tilde{u} = 0$ ). To ensure that Condition (19) remains true, the following constraint shall be satisfied:

$$\frac{\lambda_3}{L} V_{in} > \lambda_1 |x_1(t)| + |\lambda_2 x_2(t)|. \quad (20)$$

The biasing voltages of the operational amplifiers computing  $x_1(t)$  and  $x_2(t)$  are  $\pm 8$  and  $\pm 5$ , respectively. This physically limits the maximum and minimum values of  $x_1(t)$  and  $x_2(t)$ . Mathematically,  $|x_1(t)| < 8$  and  $|x_2(t)| < 5$ ; thus, by appropriate choice of design constants  $\lambda_1$ ,  $\lambda_2$  and  $\lambda_3$ , the constraint in Equation (20) is satisfied.

Case 2:

When  $\sigma \rightarrow 0^-$ , then Constrain (17) states that  $\dot{\sigma} > 0$ . This turns Equation (18) into inequality as:

$$\dot{\sigma} = \lambda_1 x_1(t) + \lambda_2 x_2(t) + \lambda_3 \left( \frac{V_{out}}{L} \tilde{u} - \frac{V_{in}}{L} \right) > 0. \quad (21)$$

The control law will turn  $u = 0$  ( $\tilde{u} = 1$ ). To ensure that condition in Inequality (21) remains true, the following constraint shall be satisfied:

$$\lambda_3 \frac{V_{out} - V_{in}}{L} > |\lambda_1 x_1(t)| + |\lambda_2 x_2(t)|. \quad (22)$$

The Inequality (22) is satisfied by an appropriate choice of design constants. It is important to notice that, if the output voltage of the converter is less than the input source voltage, then the inequality (22) is not satisfied. This requires careful selection of the initial conditions that guarantee the convergence of the state trajectories to  $\sigma = 0$ . At startup of the boost converter, this problem is solved by starting the converter in open loop and then closing the loop once the condition  $V_{out} > V_{in}$  is satisfied. Another simple way to solve the problem is by introducing a protection circuit that always ensures the control signal  $V_{con} < V_{Pramp}$  in the PWM circuit, which in return results in stable switching of the power electronic switch until the condition  $V_{out} > V_{in}$  is achieved.

## 5. Sliding Surface and Parametrization of the Controller

In order to achieve the desired dynamics of the system during sliding mode, the controller is parametrized using Ackermann's formula. When the system is sliding on the manifold  $\sigma = 0$ , then the reduced order dynamics of the system are totally described by the sliding coefficients. Rearranging Equation (8), we get:

$$\frac{d^2}{dt^2} e(t) + \frac{\lambda_2}{\lambda_3} \frac{d}{dt} e(t) + \frac{\lambda_1}{\lambda_3} e(t) = 0. \quad (23)$$

The standard second order equation is given as:

$$\frac{d^2 y(t)}{dt^2} + 2\zeta\omega_n \frac{dy(t)}{dt} + \omega_n^2 y(t) = 0. \quad (24)$$

Comparing coefficients of the Equations (23) with (24), we get:

$$\frac{\lambda_2}{\lambda_3} = 2\zeta\omega_n \quad \text{and} \quad \omega_n^2 = \frac{\lambda_1}{\lambda_3},$$

where  $\omega_n$  is the natural frequency and  $\zeta$  is the damping ratio. Recalling that the damping ratio in a linear time-invariant second order system corresponds to the response of the system, which is over damped for  $\zeta > 1$ , critically damped for  $\zeta = 1$  and under damped for  $\zeta < 1$ . In order to achieve a smooth and fast response with no overshoots, we choose  $\zeta = 1$ . Rearranging the above equation in terms of the bandwidth  $f_{bw}$  of the converter, we get:

$$\frac{\lambda_2}{\lambda_3} = 4\pi f_{bw} \quad \text{and} \quad \frac{\lambda_1}{\lambda_3} = 4\pi^2 f_{bw}^2. \quad (25)$$

For the desired bandwidth of 65 kHz, the calculations of the sliding coefficients using Equation (25) are as follows:

$$\frac{\lambda_2}{\lambda_3} = 4\pi f_{bw} = 4\pi(65k) = 816.4 \times 10^3,$$

$$\frac{\lambda_1}{\lambda_3} = 4\pi^2 f_{bw}^2 = 4\pi^2(65k)^2 = 2.6 \times 10^{13}.$$

It is important mention that the maximum allowable limits of the op-amps should be considered while parameterizing the controller. In our case, both  $V_{in}$  and  $V_{out}$  of the converter exceed the limits. This problem is solved by feeding  $V_{in}$  and  $V_{out}$  via voltage divider network with attenuation constant  $\gamma$ . For the desired output voltage of  $V_d = 24$  V, the reference voltage  $V_{ref}$  is kept as 2.5 V. Hence,  $\gamma$  is calculated as:

$$\gamma = \frac{V_{ref}}{V_d} = \frac{2.5}{24} = 0.104.$$

The combination of feedback resistor is calculated using  $\gamma$ . Selecting resistor  $R_1$  as 6.8 k $\Omega$ ,  $R_2$  is calculated as:

$$R_2 = \frac{\gamma}{1-\gamma} R_1 = \frac{0.104}{1-0.104} \times 6.8 \text{ k} = 789.2 \text{ } \Omega.$$

Using a series combination of standard value resistors, we get  $\gamma = 0.103$ . The constant  $\gamma$  modifies the feedback control Equation (13) as:

$$u_{eq} = d = \frac{\gamma V_{con}}{\gamma V_{out}} = \frac{V_{con}}{\gamma V_{out}},$$

where  $V_{con}$  is computed from Equation (14) as:

$$V_c = (\gamma V_{out} - \gamma V_{in}) + \gamma L \frac{\lambda_2}{\lambda_3} (I_{ref} - I_L) + \gamma L \frac{\lambda_1}{\lambda_3} \int (I_{ref} - I_L) dt. \quad (26)$$

Equation (26) can be expressed as:

$$V_c = (\gamma V_{out} - \gamma V_{in}) + k_1 (I_{ref} - I_L) + k_2 \int (I_{ref} - I_L) dt, \quad (27)$$

where  $k_1$  and  $k_2$  are:

$$k_1 = \gamma L \frac{\lambda_2}{\lambda_3} = 8.25, \quad (28)$$

$$k_2 = \gamma L \frac{\lambda_1}{\lambda_3} = 1.7 \times 10^6, \quad (29)$$

and  $V_{Pramp}$  is computed from Equation (15) as:

$$V_{Pramp} = \gamma V_{out}. \quad (30)$$

The output of op-amps computing  $x_1(t)$  and  $x_2(t)$  in Equation (18) are also scaled by the constant  $\gamma$  such that:

$$\begin{aligned} -0.52 &\leq x_1(t) \leq 0.52, \\ -0.83 &\leq x_2(t) \leq 0.83. \end{aligned}$$

The integrator in Equation (27) is designed using op-amp circuit, where gain  $k_2 = 1/(R_{1i}C_{1i})$ . By selecting  $C_{1i} = 100$  pF, the value of  $R_{1i}$  is calculated as:

$$R_{1i} = \frac{1}{C_{1i} \times 1.7 \times 10^6} = 5.8 \text{ k}\Omega.$$

The outer PI control loop has a proportional gain of 8.2 and an integral gain of  $1/R_{2i}C_{2i} = 5000$ . The integral gain is achieved by selecting  $C_{2i} = 10$  nF and  $R_{2i} = 20$  k $\Omega$ . In order to limit the maximum duty cycle of the power converter to 95%, a shunt regulator using TL431 with its reverse breakdown voltage adjusted at 4.8 V is placed at the output of the operational amplifier generating the control signal  $V_{con}$ . TL431 cannot be adjusted to regulate the output voltage lower than 2.5 V, hence a summing gain of 2 is introduced so that the signal  $V_{con}$  is greater than the minimum regulated voltage of TL431. This gain is then compensated in Equation (13) by amplifying the ramp peak  $V_{Pramp}$  by the same gain. The hardware implementation of  $u_{eq}$  and  $V_{Pramp}$  is given as:

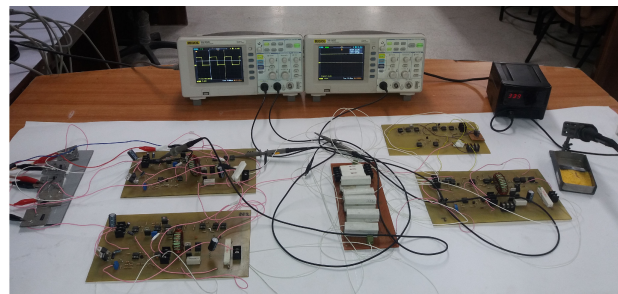
$$u_{eq} = d = \frac{2 \times V_{con}}{2 \times V_{Pramp}} = \frac{2 \times V_{con}}{2 \times \gamma V_d}. \quad (31)$$

## 6. Experimental Results and Discussion

In the experimentation, Matrix power supplies having precision to one decimal place are used to test the performance of the controller under varying input voltages and changing load conditions. The experimental results are obtained using a two channel Rigol oscilloscope having 70 MHz bandwidth and sampling rate of 1 GHz. To test the wide range operation of the boost converter, the outdoor experiment is performed using solar panels and measurements are taken with regular intervals.

The parameters of DC–DC converter are selected on the basis of 250 W output power. The inductance of the coil is 100  $\mu$ H and the output filter capacitor is of 1000  $\mu$ F. Power Metal-Oxide-Semiconductor Field-Effect Transistor (MOSFET) (IRF540) with on-resistance of 0.06  $\Omega$  and continuous drain current capability of 20 A is selected as an electronic switch. Fixed switching frequency for the sliding mode operation is selected to be 50 kHz and the experimental setup is shown in Figure 4. The efficiency of the converter at this frequency is experimentally observed to be 90.06% when delivering 7 W to the load. It is observed that, in order to ensure the efficient switching, the resistance seen by the MOSFET at its drain shall be kept less than 47  $\Omega$  so as to keep the discharge interval of body diode capacitance of the MOSFET, less than its switching interval under SMC. A reference signal of 2.5 V is generated using adjustable shunt regulator TL431 with its reference pin connected to its cathode. Due to the uni-directional nature of inductor current, it is not possible to measure it using a current transformer (CT). To measure  $I_L$ , a resistor  $R_M$  is placed in its return path. As  $I_L$  flows, a voltage  $V_M$  is developed across  $R_M$  and we measure the inductor current as:

$$I_L = \frac{V_M}{R_M}. \quad (32)$$



(a)



(b)

**Figure 4.** Experimental set-up for the proposed technique. (a) 24 V setup; (b) 110 V setup.

### 6.1. Open Loop Response

In order to emphasize the need of the feedback control, the open loop response of the system is presented in Figure 5. The converter is operated, in open loop with a PWM signal having a 50% duty ratio. The calculated output of the converter at this signal is 24 V, but the experimental output is 22.8 V, which is 1.2 V less than the calculated output. This difference occurs due to the voltage drop in the parasitic resistance of the hardware components and the connecting leads. The output further drops to 20 V when an additional load of 47  $\Omega$  is connected to the existing 82  $\Omega$  load. Hence, it may be concluded that in open loop, the output of the power converter exhibits a steady state error that changes with variation in load resistors.

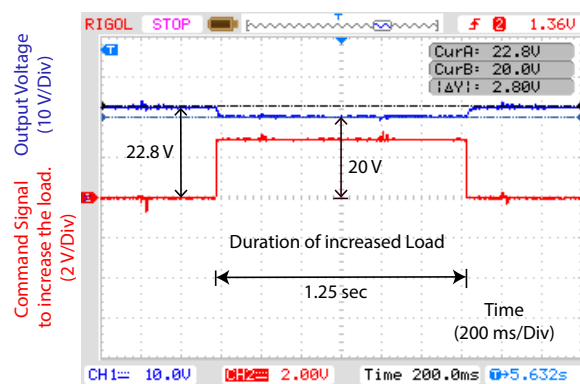


**Figure 5.** Output voltage of the boost converter in an open loop during rated load and full load.

## 6.2. Comparison with Current Mode Controller

The performance of the proposed technique is analyzed along with the conventional current-mode controller, having a PI loop each for voltage regulation and current tracking. For the sake of comparison, the bandwidth of the proposed technique is set to be the same as the current-mode controller. The circuit diagram for voltage regulation in a single source is shown in Figure 6.

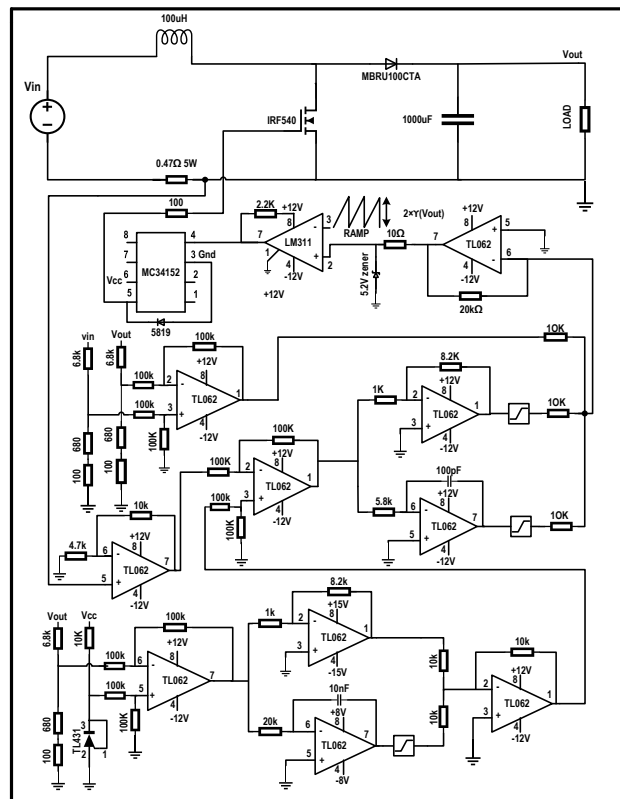


**Figure 6.** Schematic diagram of the proposed technique for voltage regulation in a single source using boost converter.

### 6.2.1. Dynamic Response

The dynamic response of the current-mode PI controller is presented in Figure 7a. The controller achieves 24 V with rise time of 41 ms and settles to final value in 80 ms. Figure 7b shows the response of the proposed fixed frequency SMC. The proposed controller has rise time of 40 ms and settling time of 75 ms. The results show an improvement of 2.5% in the rise time and 6.66% in the settling time of the closed loop system. The response is faster as compared to the current-mode PI controller due to the presence of a feedforward term in the proposed technique.

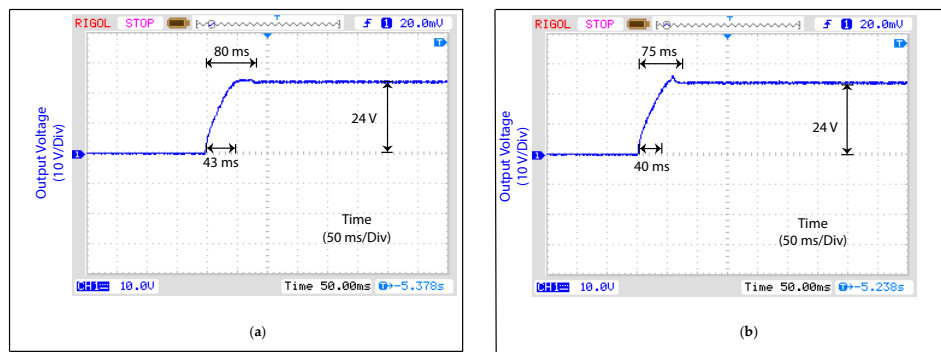


**Figure 7.** Step response of the system. (a) conventional current-mode controller; (b) fixed frequency Double Integral Sliding Mode Control (DI-SMC).

The switching sequence generated by the controller is shown in Figure 8a. The drain voltage resulting due to switching of MOSFET is shown on CH1 in Figure 8b. The CH2 in the same figure shows the inductor current. It shall be noticed that the time period of switching sequence is constant, hence the objective of fixing the switching frequency in SMC is achieved by the proposed technique.

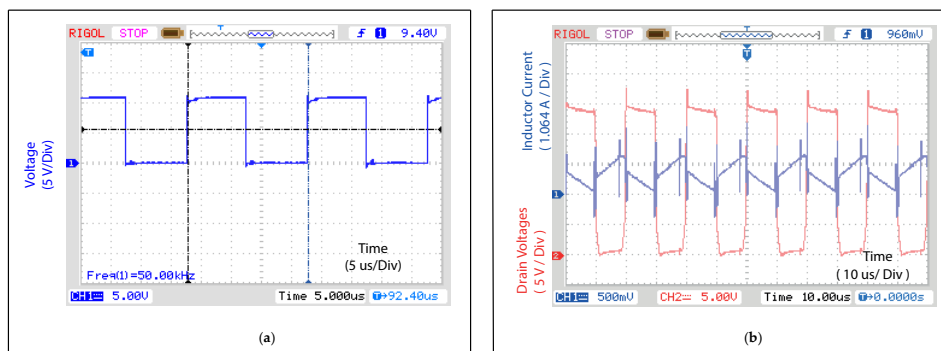


**Figure 8.** Fixed frequency operation of the converter. (a) switching signal; (b) drain voltage and inductor current.

The hardware can be easily scaled for operation at any desired output by proper selection of  $\gamma$ . The value of  $\gamma$  shall be selected such that the feedback signal does not exceed the power supply voltages of the operational amplifiers and other control circuitry. In order to observe the behavior of the controller for high voltage and large power applications, the technique is also applied to the converter with specifications shown in Table 1. The experimental setup is shown in Figure 4b where the input voltage is applied using four 12 V lead acid batteries connected in series having 200 AH current rating. The output is regulated at 110 V while delivering 1230 W to the load. Figure 9a shows the inductor current that is measured using a current to voltage conversion circuit while the dynamic response of the converter is shown in Figure 9b. For the sake of analysis, the output voltage is fed to the oscilloscope through a resistive network of 0.1 attenuation and is measured using its 10 $\times$  settings.

**Table 1.** Parameters of power converter.

Parameter	Value
Input Voltage	55 V
Output Voltage	110 V
Inductance of Coil	100 $\mu$ H
Output capacitance	1000 $\mu$ F
Max. Output power	2000 W

**Table 2.** Output voltages for variations in input.

$V_{in}$	$V_{out}$
12.1	24.0
14.5	24.0
16.0	24.0
18.1	24.0

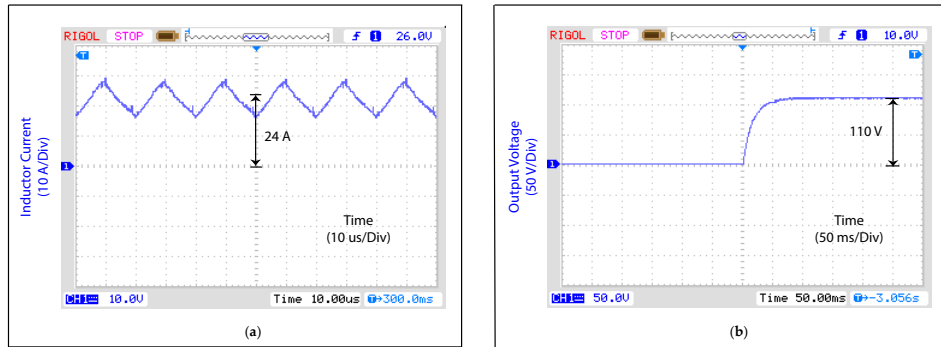


**Figure 9.** Performance of the DI-SMC during large power application. (a) inductor current; (b) step response.

### 6.2.2. Robustness of the Controller

The robustness of the controller is verified by applying a step change in load from  $82 \Omega$  to  $29.9 \Omega$ . This step change is emulated by connecting and disconnecting a  $47 \Omega$  resistor in parallel with  $82 \Omega$  load at a frequency of 10 KHz. The switching is achieved by using a Darlington paired Positive-Negative-Positive (PNP) power transistor (TIP142) whose base is driven by Negative-Positive-Negative (NPN) transistor (C828). Figure 10a shows that the conventional current-mode controller exhibits an undershoot of 4.1 V and recovers in 640 ns. Figure 10b shows that the proposed DI-SMC exhibits an under-shoot of only 2.8 V and recovers in 250 ns with no steady state error. Hence, the voltage dip during load transaction is reduced by 31.7%. This verifies the robustness of the proposed technique to a sudden change in load which is a key feature of SMC designs. The experimental setup for the proposed controller is shown in Figure 4. The proposed controller is also tested for line variations. The test is performed by changing the input voltage from  $V_{in} = 12 \text{ V}$  to  $V_{in} = 18 \text{ V}$ . The controller operates effectively and the results are summarized in Table 2.

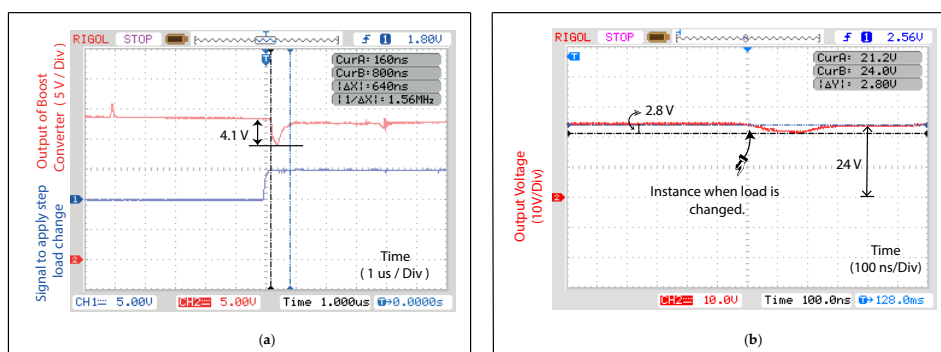


**Figure 10.** Experiment waveform of the output voltage when an additional load of  $47 \Omega$  is connected in parallel to  $82 \Omega$  load. (a) conventional current-mode controller; (b) fixed frequency DI-SMC.

### 6.3. Grid Testing for Fault Condition

The capability of the proposed technique to operate in a DC micro-grid is experimentally validated on a test rig comprising of three sources. An outer control loop based on a PI-controller provides reference current signal for the each source connected to the micro-grid. The tracking of the reference current is accomplished in each source by using a boost converter controlled by the proposed double integral type fixed frequency SMC. During the steady state condition, the bus voltage is 24 V and the currents supplied by the sources are 1.61 A, 1.63 A and 1.62 A, respectively. The system is operated at a partial load such that, if one source fails, the other two sources have sufficient power capability to fulfill the load demand. The fault in Source 2 is emulated by disconnecting its control signal. Figure 11a–c show the current of each source during the fault condition. Figure 11d shows the voltage transient at the load during the fault. The new currents supplied by Sources 1 and 3 are 2.42 A and 2.44 A, respectively, which corresponds to 0.82% error in load sharing. Hence, the load disturbances on the position of DC–DC micro-grids have been effectively addressed, confirming that the proposed technique is capable of operation even during an instantaneous increase in the load demand or in case of a fault in the connected sources.

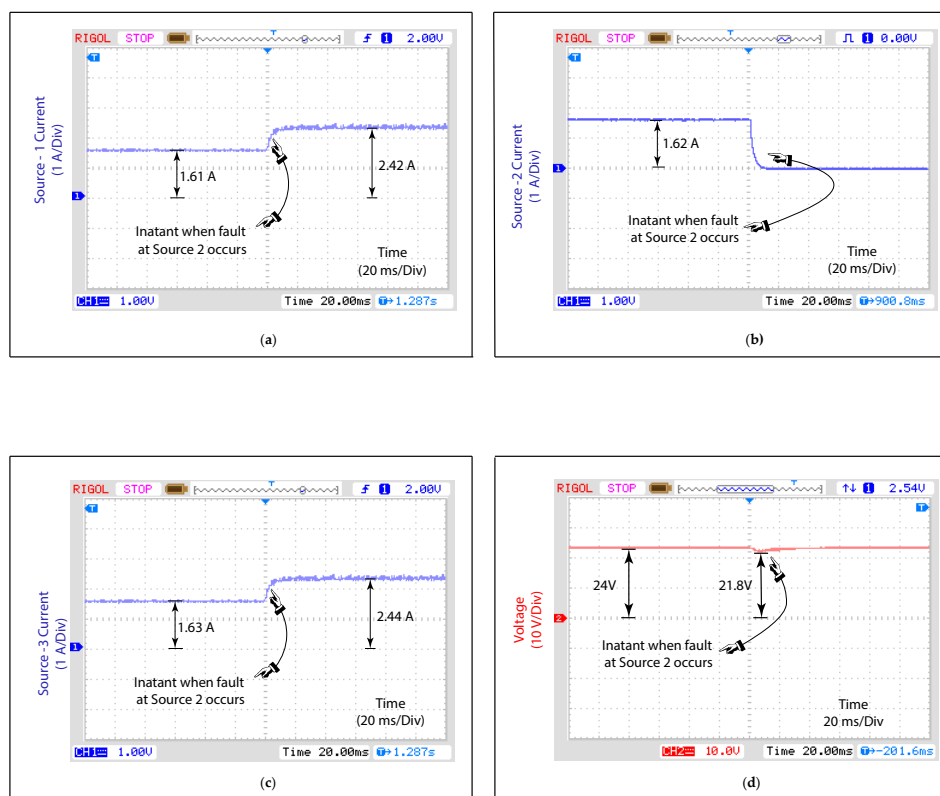


**Figure 11.** Grid operation of DI-SMC. (a) output current of Source-1; (b) output current of Source-2; (c) output current of Source-3. (d) Load voltage during fault condition.

## 7. Conclusions

In this paper, voltage regulation of DC micro-grid using fixed frequency SMC with a novel double integral type sliding manifold is proposed along with a rigorous proof for the stability of the system. The controller is tested experimentally and the results show the desired performance of the proposed technique along with providing robustness against fluctuations in input voltages and change in load conditions. A detailed discussion on parametrization of the controller, hardware design and circuit implementation is presented. The technique is also applied on a micro-grid test bench, having three sources and the results show satisfactory operation of the closed loop system. The controller is

implemented using commercially available analogue ICs which eliminated the need of using expensive analogue-to-digital data accusation cards along with phasing out the issues due to their finite sampling time. For the purpose of bench marking, the results are compared with conventional PI controller. The proposed technique improved the dynamic response of the closed loop system by reducing both, the rise time and the settling time by 2.5% and 6.7%, respectively. It is observed that a sudden voltage dip appears in the regulated voltage when an additional load is connected. This dip is reduced by 31.7% for the proposed controller as compared to that of the conventional PI controller.

The future work may be extended to the study of the proposed technique in more diverse networks including different types of power converters, controlled by various local techniques, other than the one presented in this research.

**Author Contributions:** A.R.Y. has conducted the research and written the manuscript under the supervision of M.A. A.I.B. has helped in driving mathematical expressions for the existence of the sliding mode control.

**Funding:** This research received no external funding.

**Acknowledgments:** The authors would like to thank the Capital University of Science and Technology.

**Conflicts of Interest:** The authors declare no conflict of interest.

## Abbreviations

The following abbreviations are used in this manuscript:

AC	Alternating Current
BJT	Bipolar Junction Transistor
DC	Direct Current
DGU	Distributed Generation Units
DSP	Digital Signal Processors
EMI	Electromagnetic Interference
FPGA	Field-Programmable Gate Array
LED	Light Emitting Diode
Li-ion	Lithium-ion
MOSFET	Metal Oxide Field-Effect Transistor
Ni-Cd	Nickel-Cadmium
PID	Proportional Integral Derivative
PI	Proportional Integral
PWM	Pulse Width Modulation
PV	Photo-Voltaic
RER	Renewable Energy Resources
SMC	Sliding Mode Control
$C$	Capacitance
$\gamma$	Attenuation Constant
$f_{bw}$	Bandwidth of the Converter
$u$	Control Input
$V_{con}$	Control Signal
$\zeta$	Damping Ratio
$\lambda$	Design Constants
$V_d$	Desired Output Voltage
$d$	Duty Ratio
$u_{eq}$	Equivalent Control
$e(t)$	Error Signal
$I_L$	Inductor Current
$L$	Inductor of coil
$V_{in}$	Input Voltage
$R_{load}$	Load Resistor
$V_{out}$	Output Voltage

$V_{Pramp}$	Peak Amplitude of Modulating Ramp
$I_{ref}$	Reference Current
$V_{ref}$	Reference Voltage
$\sigma$	Sliding Manifold

## References

- Díaz, N.L.; Luna, A.C.; Vasquez, J.C.; Guerrero, J.M. Centralized control architecture for coordination of distributed renewable generation and energy storage in islanded ac microgrids. *IEEE Trans. Power Electron.* **2017**, *32*, 5202–5213. [[CrossRef](#)]
- Faria, P.; Spínola, J.; Vale, Z. Distributed Energy Resources Scheduling and Aggregation in the Context of Demand Response Programs. *Energies* **2018**, *11*, 1987. [[CrossRef](#)]
- Dörfler, F.; Simpson-Porco, J.W.; Bullo, F. Breaking the Hierarchy: Distributed Control and Economic Optimality in Microgrids. *IEEE Trans. Control Netw. Syst.* **2016**, *3*, 241–253. [[CrossRef](#)]
- Jin, M.; Feng, W.; Marnay, C.; Spanos, C. Microgrid to enable optimal distributed energy retail and end-user demand response. *Appl. Energy* **2018**, *210*, 1321–1335. [[CrossRef](#)]
- Antunez, P.D.; Bishop, D.M.; Luo, Y.; Haight, R. Efficient kesterite solar cells with high open-circuit voltage for applications in powering distributed devices. *Nat. Energy* **2017**, *2*, 884. [[CrossRef](#)]
- Bhowmik, C.; Bhowmik, S.; Ray, A.; Pandey, K.M. Optimal green energy planning for sustainable development: A review. *Renew. Sustain. Energy Rev.* **2017**, *71*, 796–813. [[CrossRef](#)]
- Mohan, N.; Undeland, T.M. *Power Electronics: Converters, Applications, and Design*; John Wiley & Sons: Hoboken, NJ, USA, 2007.
- Ivanovic, Z.; Blanusa, B.; Knezic, M. Power loss model for efficiency improvement of boost converter. In Proceedings of the 2011 XXIII International Symposium on Information, Communication and Automation Technologies, Sarajevo, Bosnia and Herzegovina, 27–29 October 2011; pp. 1–6.
- Lotfi, H.; Khodaei, A. AC versus DC microgrid planning. *IEEE Trans. Smart Grid* **2017**, *8*, 296–304. [[CrossRef](#)]
- Dragicevic, T.; Vasquez, J.C.; Guerrero, J.M.; Skrlec, D. Advanced LVDC Electrical Power Architectures and Microgrids: A step toward a new generation of power distribution networks. *IEEE Electr. Mag.* **2014**, *2*, 54–65. [[CrossRef](#)]
- Wang, C.; Duan, J.; Fan, B.; Yang, Q.; Liu, W. Decentralized High-Performance Control of DC Microgrids. *IEEE Trans. Smart Grid* **2018**. [[CrossRef](#)]
- Cairoli, P.; Dougal, R.A. Fault Detection and Isolation in Medium-Voltage DC Microgrids: Coordination between Supply Power Converters and Bus Contactors. *IEEE Trans. Power Electron.* **2018**, *33*, 4535–4546. [[CrossRef](#)]
- Saleh, M.; Esa, Y.; Mohamed, A. Communication Based Control for DC Microgrids. *IEEE Trans. Smart Grid* **2018**. [[CrossRef](#)]
- Dehkordi, N.M.; Baghaee, H.R.; Sadati, N.; Guerrero, J.M. Distributed Noise-resilient Secondary Voltage and Frequency Control for Islanded Microgrids. *IEEE Trans. Smart Grid* **2018**. [[CrossRef](#)]
- Mousavi, S.Y.M.; Jalilian, A.; Savaghebi, M.; Guerrero, J.M. Coordinated control of multifunctional inverters for voltage support and harmonic compensation in a grid-connected microgrid. *Electr. Power Syst. Res.* **2018**, *155*, 254–264. [[CrossRef](#)]
- Sun, K.; Zhang, L.; Xing, Y.; Guerrero, J.M. A Distributed Control Strategy Based on DC Bus Signaling for Modular Photovoltaic Generation Systems With Battery Energy Storage. *IEEE Trans. Power Electron.* **2011**, *26*, 3032–3045. [[CrossRef](#)]
- Schonbergerschonberger, J.; Duke, R.; Round, S.D. DC-Bus Signaling: A Distributed Control Strategy for a Hybrid Renewable Nanogrid. *IEEE Trans. Ind. Electron.* **2006**, *53*, 1453–1460. [[CrossRef](#)]
- Alizadeh, E.; Birjandi, A.M.; Hamzeh, M. Decentralised power sharing control strategy in LV microgrids under unbalanced load conditions. *IET Gener. Transm. Distrib.* **2017**, *11*, 1613–1623. [[CrossRef](#)]
- Cucuzzella, M.; Trip, S.; De Persis, C.; Cheng, X.; Ferrara, A.; van der Schaft, A. A robust consensus algorithm for current sharing and voltage regulation in dc microgrids. *IEEE Trans. Control Syst. Technol.* **2018**. [[CrossRef](#)]
- Kakigano, H.; Miura, Y.; Ise, T.; Uchida, R. DC voltage control of the DC micro-grid for super high quality electric power distribution. *IEEE Trans. Ind. Appl.* **2007**, *127*, 890–897. [[CrossRef](#)]

21. Han, R.; Meng, L.; Guerrero, J.M.; Vasquez, J.C. Distributed nonlinear control with event-triggered communication to achieve current-sharing and voltage regulation in DC microgrids. *IEEE Trans. Power Electron.* **2018**, *33*, 6416–6433. [[CrossRef](#)]
22. Guerrero, J.M.; Vasquez, J.C.; Matas, J.; de Vicuna, L.G.; Castilla, M. Hierarchical Control of Droop-Controlled AC and DC Microgrids 2014; A General Approach Toward Standardization. *IEEE Trans. Ind. Electron.* **2011**, *58*, 158–172. [[CrossRef](#)]
23. Wai, R.J.; Shih, L.C. Design of voltage tracking control for DC–DC boost converter via total sliding-mode technique. *IEEE Trans. Ind. Electron.* **2011**, *58*, 2502–2511. [[CrossRef](#)]
24. Shirazi, M.; Zane, R.; Maksimovic, D. An autotuning digital controller for DC–DC power converters based on online frequency-response measurement. *IEEE Trans. Power Electron.* **2009**, *24*, 2578–2588. [[CrossRef](#)]
25. Guo, L.; Hung, J.Y.; Nelms, R.M. Evaluation of DSP-Based PID and Fuzzy Controllers for DC 2013; DC Converters. *IEEE Trans. Ind. Electron.* **2009**, *56*, 2237–2248. [[CrossRef](#)]
26. Lee, M.; Chen, D.; Huang, K.; Liu, C.W.; Tai, B. Modeling and Design for a Novel Adaptive Voltage Positioning (AVP) Scheme for Multiphase VRMs. *IEEE Trans. Power Electron.* **2008**, *23*, 1733–1742. [[CrossRef](#)]
27. Onwuchekwa, C.N.; Kwasinski, A. Analysis of Boundary Control for Buck Converters With Instantaneous Constant-Power Loads. *IEEE Trans. Power Electron.* **2010**, *25*, 2018–2032. [[CrossRef](#)]
28. Galvez, J.M.; Ordóñez, M.; Luchino, F.; Quaiçoe, J.E. Improvements in Boundary Control of Boost Converters Using the Natural Switching Surface. *IEEE Trans. Power Electron.* **2011**, *26*, 3367–3376. [[CrossRef](#)]
29. Kirshenboim, O.; Peretz, M.M. Stability Analysis of Boundary and Hybrid Controllers for Indirect Energy Transfer Converters. *IEEE Trans. Power Electron.* **2016**, *31*, 3360–3371. [[CrossRef](#)]
30. Linares-Flores, J.; Méndez, A.H.; García-Rodríguez, C.; Sira-Ramírez, H. Robust Nonlinear Adaptive Control of a Boost Converter via Algebraic Parameter Identification. *IEEE Trans. Ind. Electron.* **2014**, *61*, 4105–4114. [[CrossRef](#)]
31. Cavanini, L.; Cimini, G.; Ippoliti, G.; Bemporad, A. Model predictive control for pre-compensated voltage mode controlled DC–DC converters. *IET Control Theory Appl.* **2017**, *11*, 2514–2520. [[CrossRef](#)]
32. Kim, S.K.; Park, C.R.; Kim, J.S.; Lee, Y.I. A stabilizing model predictive controller for voltage regulation of a DC/DC boost converter. *IEEE Trans. Control Syst. Technol.* **2014**, *22*, 2016–2023. [[CrossRef](#)]
33. Karamanakos, P.; Geyer, T.; Manias, S. Direct voltage control of dc–dc boost converters using enumeration-based model predictive control. *IEEE Trans. Power Electron.* **2014**, *29*, 968–978. [[CrossRef](#)]
34. Wang, Y.X.; Yu, D.H.; Kim, Y.B. Robust Time-Delay Control for the DC–DC Boost Converter. *IEEE Trans. Ind. Electron.* **2014**, *61*, 4829–4837. [[CrossRef](#)]
35. Utkin, V.I. Sliding mode control design principles and applications to electric drives. *IEEE Trans. Ind. Electron.* **1993**, *40*, 23–36. [[CrossRef](#)]
36. Calvente, J.; El Aroudi, A.; Giral, R.; Cid-Pastor, A.; Vidal-Idiarte, E.; Martínez-Salamero, L. Design of Current Programmed Switching Converters Using Sliding-Mode Control Theory. *Energies* **2018**, *11*, 2034. [[CrossRef](#)]
37. Delghavi, M.B.; Yazdani, A. Sliding-Mode Control of AC Voltages and Currents of Dispatchable Distributed Energy Resources in Master-Slave-Organized Inverter-Based Microgrids. *IEEE Trans. Smart Grid* **2017**. [[CrossRef](#)]
38. Pilloni, A.; Pisano, A.; Usai, E. Robust Finite-Time Frequency and Voltage Restoration of Inverter-Based Microgrids via Sliding-Mode Cooperative Control. *IEEE Trans. Ind. Electron.* **2018**, *65*, 907–917. [[CrossRef](#)]
39. Dou, C.; Zhang, B.; Yue, D.; Zhang, Z.; Xu, S.; Hayat, T.; Alsaedi, A. A Novel Hierarchical Control Strategy Combined with Sliding Mode Control and Consensus Control for Islanded Micro-grid. *IET Renew. Power Gener.* **2018**, *12*, 1012–1024. [[CrossRef](#)]
40. Fu, Y.; Zhang, H.; Mi, Y.; Huang, L.; Li, Z.; Wang, J. Control strategy of DFIG in hybrid micro-grid using sliding mode frequency controller and observer. *IET Gener. Transm. Distrib.* **2018**, *12*, 2662–2669. [[CrossRef](#)]
41. Shinde, U.K.; Kadwane, S.G.; Gawande, S.P.; Reddy, M.J.B.; Mohanta, D.K. Sliding Mode Control of Single-Phase Grid-Connected Quasi-Z-Source Inverter. *IEEE Access* **2017**, *5*, 10232–10240. [[CrossRef](#)]
42. Zhu, Y.; Fei, J. Adaptive Global Fast Terminal Sliding Mode Control of Grid-connected Photovoltaic System Using Fuzzy Neural Network Approach. *IEEE Access* **2017**, *5*, 9476–9484. [[CrossRef](#)]
43. Ghiasi, M.I.; Golkar, M.A.; Hajizadeh, A. Lyapunov Based-Distributed Fuzzy-Sliding Mode Control for Building Integrated-DC Microgrid With Plug-In Electric Vehicle. *IEEE Access* **2017**, *5*, 7746–7752. [[CrossRef](#)]
44. Utkin, V. Sliding mode control of DC/DC converters. *J. Frankl. Inst.* **2013**, *350*, 2146–2165. [[CrossRef](#)]

45. Teja, A.R.; Chakraborty, C.; Pal, B.C. Disturbance Rejection Analysis and FPGA based Implementation of a Second Order Sliding Mode Controller fed Induction Motor Drive. *IEEE Trans. Energy Convers.* **2018**, *33*, 1453–1462. [[CrossRef](#)]
46. Yang, B.; Yu, T.; Shu, H.; Dong, J.; Jiang, L. Robust sliding-mode control of wind energy conversion systems for optimal power extraction via nonlinear perturbation observers. *Appl. Energy* **2018**, *210*, 711–723. [[CrossRef](#)]
47. Tan, S.C.; Lai, Y.M.; Cheung, M.K.H.; Tse, C.K. On the practical design of a sliding mode voltage controlled buck converter. *IEEE Trans. Power Electron.* **2005**, *20*, 425–437. [[CrossRef](#)]
48. Pareschi, F.; Rovatti, R.; Setti, G. EMI Reduction via Spread Spectrum in DC/DC Converters: State of the Art, Optimization, and Tradeoffs. *IEEE Access* **2015**, *3*, 2857–2874. [[CrossRef](#)]
49. Mohanty, P.R.; Panda, A.K. Fixed-Frequency Sliding-Mode Control Scheme Based on Current Control Manifold for Improved Dynamic Performance of Boost PFC Converter. *IEEE J. Emerg. Sel. Top. Power Electron.* **2017**, *5*, 576–586. [[CrossRef](#)]
50. He, Y.; Luo, F. Sliding-mode control for dc–dc converters with constant switching frequency. *IEE Proc. Control Theory Appl.* **2006**, *153*, 37–45. [[CrossRef](#)]
51. Ye, J.; Malysz, P.; Emadi, A. A fixed-switching-frequency integral sliding mode current controller for switched reluctance motor drives. *IEEE J. Emerg. Sel. Top. Power Electron.* **2015**, *3*, 381–394.
52. Abeywardana, D.B.W.; Hredzak, B.; Agelidis, V.G. A fixed-frequency sliding mode controller for a boost-inverter-based battery-supercapacitor hybrid energy storage system. *IEEE Trans. Power Electron.* **2017**, *32*, 668–680. [[CrossRef](#)]
53. Gao, M.; Wang, D.; Li, Y.; Yuan, T. Fixed frequency pulse-width modulation based integrated sliding mode controller for phase-shifted full-bridge converters. *IEEE Access* **2018**, *6*, 2181–2192. [[CrossRef](#)]
54. Chincholkar, S.H.; Chan, C.Y. Design of fixed-frequency pulsewidth-modulation-based sliding-mode controllers for the quadratic boost converter. *IEEE Trans. Circuits Syst. II Express Briefs* **2017**, *64*, 51–55. [[CrossRef](#)]
55. Sira-Ramirez, H. Sliding-mode control on slow manifolds of DC-to-DC power converters. *Int. J. Control* **1988**, *47*, 1323–1340. [[CrossRef](#)]
56. Shahir, F.M.; Babaei, E.; Farsadi, M. Extended Topology for Boost DC–DC Converter. *IEEE Trans. Power Electron.* **2018**. [[CrossRef](#)]
57. Alsmadi, Y.M.; Utkin, V.; Haj-ahmed, M.A.; Xu, L. Sliding mode control of power converters: DC/DC converters. *Int. J. Control* **2017**, 1–22. [[CrossRef](#)]
58. Kokotovic, P.V.; O'malley, R.; Sannuti, P. Singular perturbations and order reduction in control theory—An overview. *Automatica* **1976**, *12*, 123–132. [[CrossRef](#)]
59. Kokotović, P.V. Applications of singular perturbation techniques to control problems. *SIAM Rev.* **1984**, *26*, 501–550. [[CrossRef](#)]
60. Utkin, V.; Guldner, J.; Shi, J. *Sliding Mode Control in Electro-Mechanical Systems*; CRC Press: Boca Raton, FL, USA, 2009; Volume 34.
61. Tan, S.C.; Lai, Y.; Tse, C.K. Indirect sliding mode control of power converters via double integral sliding surface. *IEEE Trans. Power Electron.* **2008**, *23*, 600.
62. Sira-Ramirez, H.; Ilic, M. A geometric approach to the feedback control of switch mode DC-to-DC power supplies. *IEEE Trans. Circuits Syst.* **1988**, *35*, 1291–1298. [[CrossRef](#)]

